https://doi.org/10.1038/s44306-024-00054-z

Recent progress on controlling spin-orbit torques by materials design

Guiping Ji[1,2], Yuejie Zhang[1,2], Yahong Chai[1,2] & Tianxiang Nan[1] ✉

Spin-orbit torques (SOTs) provide an energy-efficient approach for the electrical manipulation of magnetization, pivotal for next-generation information storage and processing devices. SOTs can be generated via various mechanisms, such as spin Hall effect, Rashba-Edelstein effect, orbital Hall effect, magnons, and spin swapping. SOTs-based devices hold potential advantages over spin-transfer torque (STT) devices, including low power consumption, enhanced durability, and a broader selection of applicable materials for both SOT generation and excitation. Despite the discovery of numerous materials capable of generating significant SOTs, achieving efficient and deterministic field-free switching of perpendicular magnetization remains a critical challenge, which is essential for the practical deployment of SOT in high-density magnetic memories. This review highlights recent progress in controlling SOTs through innovative materials design, encompassing strategies such as strain engineering of the spin Hall angle, interfacial engineering of the spin transmissivity and topological surface states, and symmetry engineering to achieve deterministic field-free switching of perpendicular magnetization. By exploring these effective methods for manipulating SOTs, this review aims to lay the groundwork for the development of optimized spintronics devices and applications.

The manipulation of magnetization is a critical aspect of spintronic research[1–4], driving development of spintronic devices for information storage[5–7],sensing[8] and processing applications[9–11], such as magnetic random-access memory (MRAM)[12–18], nano-oscillators[19–25], neuromorphic computing devices[26–30], magnetic sensors[8,31–34], and so on. Previously, Oersted field generated by charge current and current-induced spin transfer torque (STT)[35–37] were employed to manipulate magnetization. In recent years, current-induced spin–orbit torques (SOTs)[38–41] emerged as a more effective approach for manipulating magnetization. SOTs can be generated via various mechanisms, such as spin Hall effect (SHE)[42–46], Rashba–Edelstein effect[47–52], orbital Hall effect[53–58], magnons[59–66] and spin swapping[67–70]. In the case of spin Hall effect, an in-plane transverse charge current in the spin source materials generates a longitudinal pure spin current, which transports spin angular momentum with polarization $\boldsymbol{\sigma}$ into adjacent ferromagnetic(FM) layer, exerting torques on the magnet. As for Rashba–Edelstein effect, spin accumulation is created by a charge current in a two-dimensional electron gas with SOC and magnetic exchange, exerting torque on adjacent magnetization. The produced spin–orbit torque could be decomposed into two components that are perpendicular to each other, a anti-damping torque $\tau_{AD}\,\mathbf{m}\times(\mathbf{m}\times\boldsymbol{\sigma})$ and a field-like torque $\tau_{FL}\,\mathbf{m}\times\boldsymbol{\sigma}$, where $\mathbf{m}$ is the unit vector of the magnet[6,13,38]. To evaluate the charge-to-spin efficiency of a spin source material, the merits of figure, spin Hall angle (SHA) θ_{SH} is defined as[6,13,38]

$$\theta_{SH}=\frac{2e}{\hbar}\frac{j_s}{j_c} \tag{1}$$

where j_c is the charge current density in the spin source material, j_s is the generated spin current, e is the electron charge, and $\hbar$ is the reduced Planck constant. Considering that spin scattering and spin loss during the transportation could reduce the amount of spin angular momentum that arrives the adjacent ferromagnetic layer, another index SOT efficiency θ_{SOT} is used, which is defined as

$$\theta_{SOT}=T_{int}\theta_{SH} \tag{2}$$

where θ_{SH} is the SHA, and T_{int} is the spin transparency[71–73].

SOTs offer several advantages on manipulating magnetization compared to STT[6,74]. Firstly, benchmark SOT materials show higher charge-to-spin conversion efficiency, which results in lower power consumption in the SOTs-based devices[6,74]. Secondly, the configuration of SOT devices are three-terminal structures with separate paths for writing and reading, giving arise to longer duration[1–6]. Thirdly, SOT materials are not limited to

[1]School of Integrated Circuits, Beijing National Research Center for Information Science and Technology, Tsinghua University, Beijing, China. [2]These authors contributed equally: Guiping Ji, Yuejie Zhang, Yahong Chai ✉e-mail: nantianxiang@mail.tsinghua.edu.cn

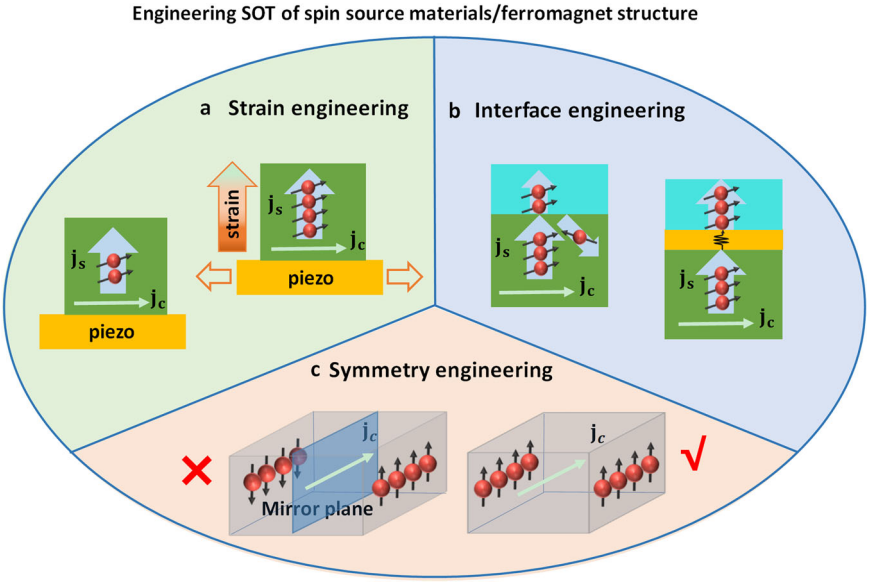

Fig. 1 | Methods of controlling SOTs in spin source/FM structures. a Strain engineering. Application of strain from the piezo substrate onto the film enhances the spin current. **b** Interface engineering. Inserting an oxide layer into the spin source/FM structure increases the transparency of the spin current. **c** Symmetry engineering. Spin current with *z*-polarization is prohibited by the mirror symmetry (left), and allowed when no mirror plane appears (right).

ferromagnet(FM), they also include ferrimagnets[75–78] and antiferromagnets[79–82] opening up new possibilities for novel spintronic devices.

To date, plenty of materials are identifed as capable of generating significant SOTs, including heavy metals(HM)[38–40,76,77], oxides[83,84], topological semimetals(TSM)[85,86] and topological insulators(TI)[87–92]. However, acquirng SOT materials with larger SOT efficiency and electronic conductivity for energy-effiecient application is still challenging[93–95]. In addition, since out-of-plane magnetization is preferred in application due to its good miniaturization, deterministic switching of the out-of-plane magnetization is essential, which can be realized through SOT generated by z-polarized spin current[39,40,95–100]. However, this unconventional SOT is generally prohibited by mirror symmetry in common spin source materials, and symmetry breaking is required for generating SOT. To address these two challenges, researchers have developed strategies for controlling both the magnitude and polarization of SOTs through materials engineering. These strategies include: (1) Strain engineering of the spin Hall angle, (2) Interfacial engineering of the spin transmissivity and topological surface states, and (3) Symmetry engineering to achieve deterministic field-free switching of out-of-plane magnetization (see Fig. 1). In this review we aim to focus on recent research works that control SOTs by the above methods.

Strain engineering

Strain engineering has emerged as a potent tool for modulating material properties that are coupled with crystal structure, such as magnetic anisotropy[101–106], electronic transportation[107], optical properties[108] and spin Hall angle[109–111].

The approaches for applying strain could be catogarized into static strain and reconfigurable strain. Static strain is typically implemented in single crystalline thin films through hetero-epitaxy on single crystal substrates. The resulting strain originates from the lattice mismatch between the film and the substrate, profoundly affecting the film's properties. Importantly, epitaxial strain from the substrate can not only alter the lattice constant of the film but also its crystalline symmetry. Reconfigurable strain can be achieved using piezoelectric substrates or flexible substrates. In this approach, deformation of substrates induces stress on the films, allowing for dynamic adjustments to the strain effects on the material properties. Additionally, this also offers a versatile platform to investigate the strain effect on the spin-Hall effect.

Static strain engineering

Static strain engineering leverages the lattice mismatch between the film and the substrate, typically kept below 5%[112,113], to prevent excessive strain accumulation at the interface that could lead to hetero-epitaxy failure[114,115].

One of the model system to study the strain effect is the transition metal oxides (TMOs). In TMOs, the intricate interplay between spin-orbit coupling and the electron correlation generates substantial Berry curvature. This, in turn, gives rise to notable intrinsic spin Hall effect[83]. Notable enhancements in SOT have been observed under strain engineering within these materials.

For instance, SrIrO3, a 5d transition-metal oxide, is found to have an enhanced SHA under strain engineering. In the NiFe/$SrIrO_3$ heterostructures grown on $SrTiO_3$ substrates[84] (Fig. 2a–c), an increase in SHA from 0.2 to 0.5 was observed via spin-torque ferromagnetic resonance (ST-FMR) measurement as the SrIrO3 thickness increased from 10 to 15 unit cells (Fig. 2c)[84], correlating with a crystal symmetry transition from tetragonal to orthorhombic. This change is evidenced by the enhanced orthorhombicity a_o/b_o (ratio of the lattice parameters) (Fig. 2b). Symmetry analysis and density functional theory (DFT) calculation have shown that SHA varies with crystal phase of $SrIrO_3$; the orthorhombic phase exhibits narrow t_{2g} bands with extensive band crossing, resulting in a higher SHA, while the strained tetragonal phase shows wide t_{2g} bands with less band crossing and a reduced SHA.

The influence of crystal symmetry on spin Hall conductivity σ_{SH} (SHC, defined as the product of SHA θ_{SH} and charge conductivity σ_c, $\sigma_{SH}=\theta_{SH}\cdot\sigma_c$) is also evident in $SrRuO_3$[116–119]. $SrRuO_3$ film, epitaxially grown on $KTaO_3$(KTO) substrates with large tensile strain (Fig. 2d), developed orthorhombic phase and had SHA as large as 0.154 (Fig. 2e)[116], whereas compressively strained $SrRuO_3$ thin film on $NdGaO_3$(NGO) substrates present tetrahedral phase with a reduced SHA of ~0.015, ----an order of magnitude smaller (Fig. 2e)[116]. Similar trends were also confirmed by a different research group, which reported that the altering the strain from compressive to tensile via epitaxial growth could enhance the SOT efficiency of SrRuO3 thin films from 0.04 to 0.89, where the crystal structure was tuned from tetrahedral to orthorhombic (Fig. 2g). Although the trend of SHA changes in $SrRuO_3$ due to epitaxial strain is consistent across the above mentioned two works, the measured value of the SHA vary significantly. This discrepancy could be attributed to several factors, including difference in thickness of the heterostructures, sample quality or disparities in interfacial spin transmission. It's a commonly known that epitaxial strain in thin film would decrease with growing film thickness due to strain relaxation. This effect has been extensively studied[120] and demonstrates a significant thickness dependence of spin and electronic

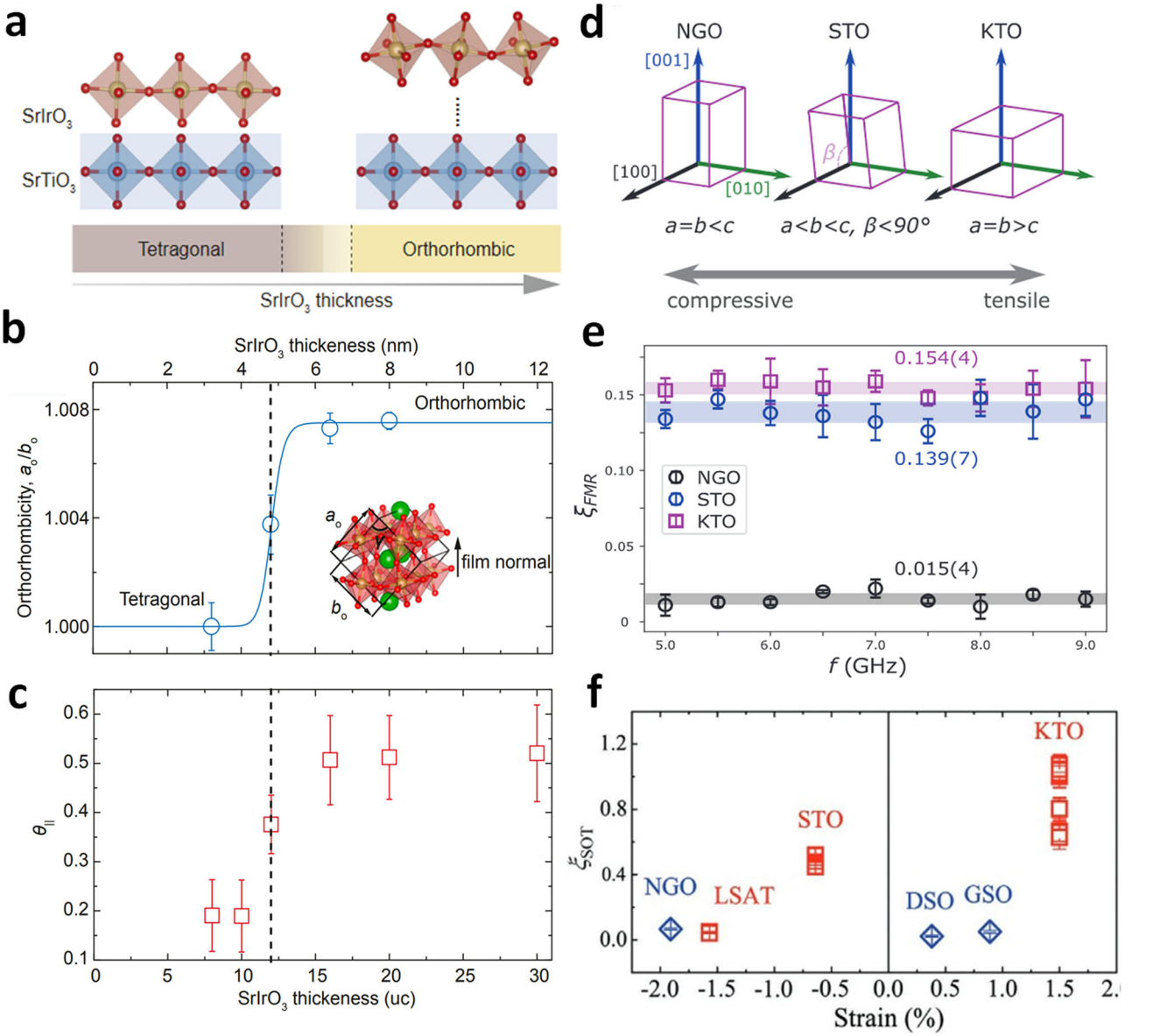

Fig. 2 | Static strain engineering via hetero-epitaxy. a–c $SrIrO_3$[84]: **a** Schematic of thickness dependence of octahedral rotation in $SrIrO_3$. **b** Thickness dependence of orthorhombicity a_o/b_o. **c** Thickness dependence of SHA in Py/$SrIrO_3$. **d–f** $SrRuO_3$[116,119]: **d** Schematic illustration of the effects of epitaxial strain on the lattice parameters of $SrRuO_3$[116]. **e** SOT efficiency of $SrRrO_3$ on $KTaO_3$(KTO), $SrTiO_3$(STO), and $NdGaO_3$(NGO) substrates[116]. **f** SOT efficiency of $SrRrO_3$ on $NdGaO_3$(NGO), $(LaAlO_3)_{0.3}(Sr_2TaAlO_6)_{0.7}$(LSAT), $SrTiO_3$(STO), $NdGaO_3$(NGO), $DyScO_3$(DSO), $GdScO_3$(GSO), and $KTaO_3$(KTO)[119].

properties in tensile-strained $SrRuO_3$ thin films. Additionally, the type of single crystal oxide substrate used can induce different artifact signals in SOT measurements, particularly in ST-FMR experiments. These artifacts can substantially influence the interpretations of strain effects on the spin-Hall effect, highlighting the need for careful consideration of experimental conditions and substrate choice in SOT research[121].

Reconfigurable strain

Under epitaxial strain, which is discrete and limited by the mismatch condition of hetero-epitaxy, reconfigurable strain allows for the application of strain in a larger scale and/or in a continuous manner[122,123].This method utilizes piezoelectric substrates or flexible substrates that can be mechanically deformed by compressing, stretching or bending. Consequently, thin films grown on these substrates adapt to the deformation, resulting in dynamically adjustable strain. Recent studies have demonstrated significant enhancements of SOT in heavy metals using reconfigurable strain engineering.

For example, in a CoFeB/Pt/PMN-PT(011) hybrid structure[124], as shown in Fig. 3a, piezoelectric strain has shown to not only modulate SOT efficiency (Fig. 3b), but also to induce an effective magnetic anisotropy and rotate the easy axis (Fig. 3c). This modification facilitates the in-plane magnetization switching and can significantly reduce the switching time by a factor of 3.

In Pt/Co bilayers, applying tensile strain along the current axis enhanced the spin Hall efficiency from 0.07 to 0.1, as shown in Fig. 3d–f[125], with 78% of the enhancement retained even after removing the strain. A linear relationship was observed between tensile strain and spin Hall efficiency, attributed to increased spin-dependent collision between the conduction electrons and ions.

Further in W/CoFeB/MgO multilayers (Fig. 3g, h)[126], both compressive and tensile strains modulated the anti-damping torque in W, enhancing it by a factor of 2 under 0.03% tensile strain, as shown in (Fig. 3g). First principle calculation revealed a strain-induced crystal symmetry transformation from

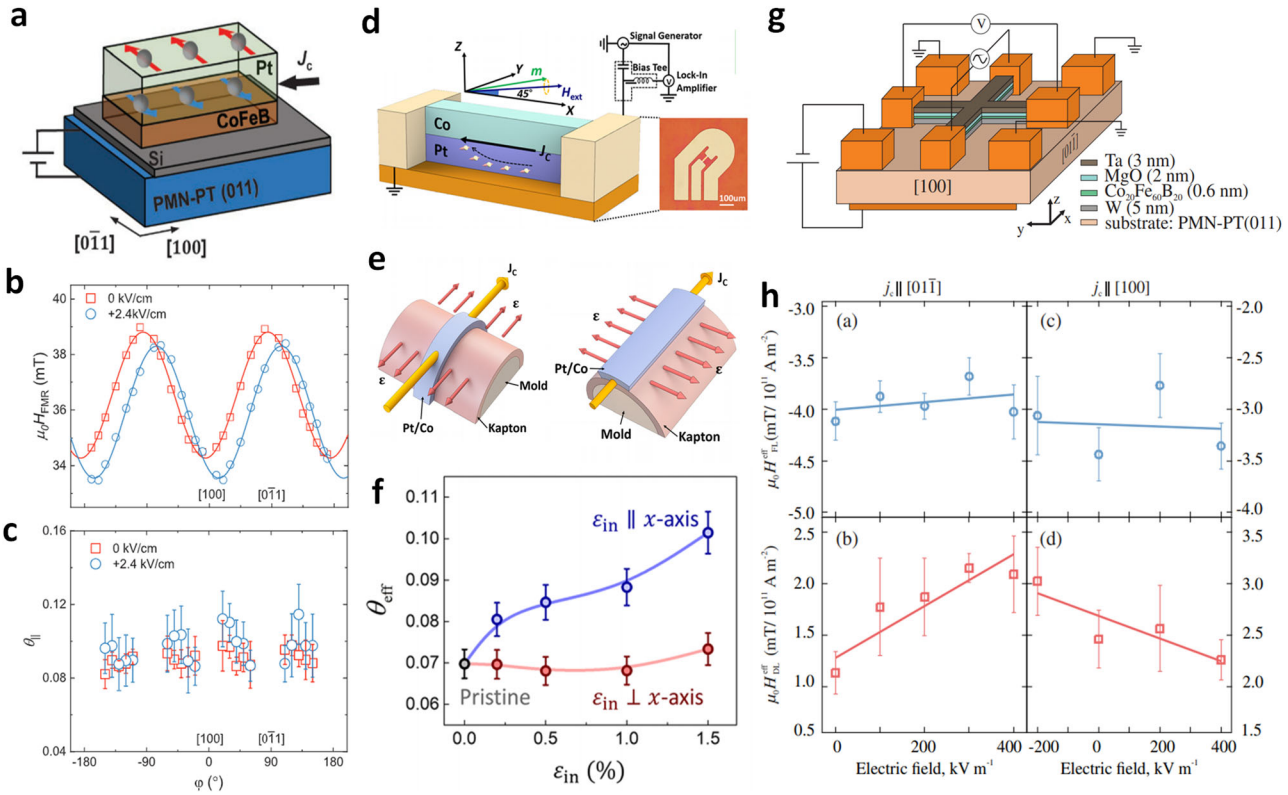

Fig. 3 | Reconfigurable strain engineering. a–c Pt/piezoelectric[124]: a Geometry of CoFeB/Pt/PMN-PT(011) device. **b** Resonance field H_{FMR} as a function of in-plane magnetic field angle for different applied electric (**c**) spin Hall angle of CoFeB/Pt/PMN-PT device. **d–f** Pt/Co bilayer system[125]: **d** Schematic illustration of a Pt/Co bilayer for the ST-FMR measurement. **e** Schematic of strain application onto the sample. **f** Spin Hall efficiency as a function of in situ tensile strain. **g, h** W/piezoelectric[126]: **g** Schematic of the Ta/MgO/CoFeB/W/PMN-PT(011) Hall bar (**h**) FL and DL SOT effective fields under compressive (left) or tensile (right) strain.

fourfold C_{4v} to twofold C_{2v}, resulting in a redistribution of the d-states of the conduction electrons and leading to enhanced intrinsic spin Hall effect.

Reconfigurable strain is not limited by the constraints of hetero-epitaxy, allowing for strain modulation even in polycrystalline SOT materials. This capability has been exploited to enhance the spin Hall angle (SHA) in polycrystalline heavy metals with strong spin-orbit coupling (SOC), further demonstrating the utility of reconfigurable strain engineering in advancing SOT technologies[125,126].

Interface engineering

Interface engineering represents a pivotal approach in enhancing the effective SOT efficiency in the heterostructures. Firstly, it improves spin transparency within the spin source/ferromagnet (FM) layer interfaces, crucial for efficient spin current transmission and effective manipulation of magnetization. Secondly, interface engineering serves to protect and stabilize topological surface states in the topological materials/FM heterostructure, which are essential for leveraging the unique properties of topological materials in spintronic devices.

Enhancement of spin transparency

Interface engineering plays a crucial role in improving SOT efficiency by enhancing spin transparency in heavy metal (HM)/ferromagnet (FM) heterostructures. In these heterostructures, a pure spin current, generated via SHE, transports across the interface to apply torques onto the adjacent magnetic layers. The transmittivity of this spin current transport across an interface is evaluated by the interfacial spin transparency, which includes contributions from spin backflow (SBF) T_{int}^{SBF} and spin memory loss (SML) T_{int}^{SML}[71,73,127,128]. The SBF refers to the back diffusion of the spin current due to spin scattering at the interface, and the SML involves the flipping of spins when the spin current crosses the interface due to the interfacial spin-orbit coupling. The total spin transparency T_{int}^{SBF}, T_{int}^{SML} and the SML T_{int}^{SML} could be expressed as,

$$T_{int} = T_{int}^{SBF} \times T_{int}^{SML} \tag{3}$$

$$T_{int}^{SBF} = \frac{G_{HM/FM}^{\downarrow\uparrow}}{G_{HM/FM}^{\downarrow\uparrow} + \frac{G_{HM}}{2}} \tag{4}$$

$$T_{int}^{SML} = \left(1 + \frac{G_{SML}^{\downarrow\uparrow}}{G_{HM/FM}^{\downarrow\uparrow} + \frac{G_{HM}}{2}}\right)^{-1} \tag{5}$$

where $G_{HM/FM}^{\downarrow\uparrow}$ is the bare spin-mixing conductance of the HM/FM interface[71,128], G_{SML} is the effective spin memory loss (SML) conductance of the interface, and $G_{HM} = 1/\rho_{xx}\lambda_s$ is spin conductance of the HM, ρ_{xx} is the resistivity of the HM and λ_s is the spin diffusion length of the HM. Improving the spin transparency T_{int} would lead to an enhanced SOT efficiency. And engineering the HM/FM interface, such as oxidizing the interface or incerting an oxide layer to the interface, is found to effectively improve the spin transparency. For instance, increasing the oxygen concentration in the W layer of the SiO_2/W(O)/CoFeB/TaN structure[129], led to a substantial rise in SOT efficiency, peaking at an oxygen concentration of 12.1%. The enhancement of SOT efficiency was considered to originate from the oxygen interface regulation. In another work, the SOT efficiency of the CuO_x/Py

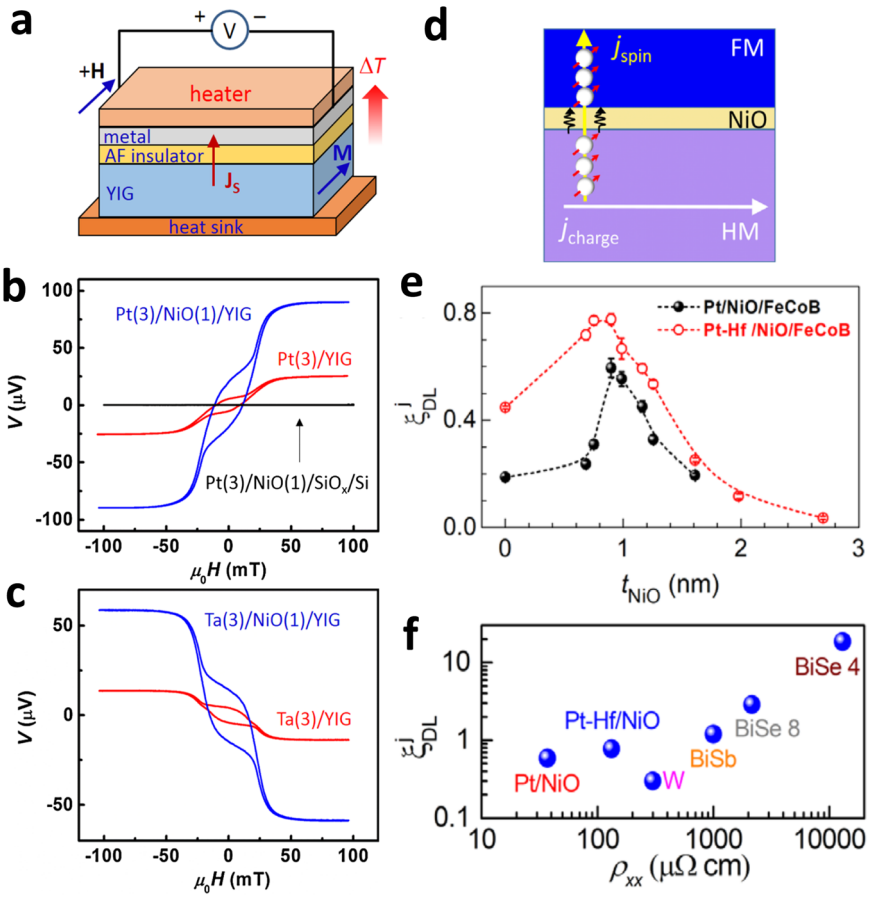

Fig. 4 | The engineering of spin–orbit torque efficiency by coupling to oxides. **a**–**c** Spin Seebeck experiment in HM/NiO/YIG: **a** Schematic diagram of the Spin Seebeck experiment for the HM/NiO/YIG structure[131]. **b**, **c** Inserting 1 nm of NiO into Pt/YIG and Ta/YIG structures can significantly increase the Spin Seebeck voltage[131]. **d**–**f** HM/NiO/CoFeB[132]: **d** Schematic of the HM/NiO/FM devices. **e** Spin Hall efficiency varies with NiO thickness[132]. **f** Comparison on estimated power of HM/NiO and other typical SOT materials[132].

bilayers was improved by changing the oxygen concentration[130], which was also attributed to the interfacial regulation of oxygen.

Insertion of an oxide layer into the HM/FM structure is also found to influence the SOT efficiency. For instance, incerting an antiferromagnetic NiO layer into the Pt/YIG interface increases the spin current, which is generated via spin Seebeck effec and measured via inverse spin Hall effect, up to an order of magnitude (Fig. 4a–c)[131]. This enhancement is attributed to the presence of the spin fluctuation in the NiO layer, which amplifies the spin current transmission, especailly at temperature that is near Néel temperature. In the Pt/NiO/FeCoB structure, the insertion of approximately 1 nm thick NiO layer markedly enhanced spin transparency (Fig. 4e–f)[132]. However, when the NiO layer's thickness exceeded 1 nm, a decline in SOT efficiency was observed, likely due to the limited spin diffusion length of NiO. Contrastingly, in the Bi_2Se_3/NiO/NiFe, there is an enhancement of the SOT efficiency at NiO thickness of ~20 nm, which can be attributed to the presence of the magnon-mediated spin torque[62].

Engineering of topological surface states

Engineering the surface states of spin source materials, especially in topological materials, is a crucial strategy for enhancing SOTs. The significant SOTs in these materials predominantly originate from the spin-momentum locking due to the presence of their surface states[133]. However, challenges arise in maintaining the integrity of these states when interfaced with ferromagnetic layers (FM). For instance, in the heterostructure of Bi_2Se_3/Ni(Co)[134], the intrinsic topological surface state of Bi_2Se_3 was disrupted. Detailed band structure analysis using density functional theory calculation and tight binding model showed discrepancies in work functions led to the shifting of topological states below the Fermi level, merging with the metallic bands of Ni(Co) and thus degrading the spin-helical structure. This phenomenon was corroborated in studies with an elemental topological Dirac semi-metal α-Sn, where angle-resolved photoelectron spectroscopy (ARPES) indicated the destruction of topological surface states upon deposition of a thin Fe layer of 0.9 Å (Fig. 5a)[135]. To preserve these critical states, several strategies have been implemented. In α-Sn structures, insertion a thin layer of Ag on the α-Sn film not only protected the Dirac cone from disruption (Fig. 5a), but also enhanced spin current absorption capabilities, evidenced by significantly increased Gilbert damping (Fig. 5b)[136]. Further, this Ag layer insertion in an α-Sn/CoFeB structure facilitated effective magnetization switching by maintaining the topological states (Fig. 5c)[86].

Substituting the ferromagnetic metallic layer with a ferromagnetic insulating layer has also shown promise in preserving topological states. In $Bi_2Se_3/BaFe_{12}O_{19}$ structure[90], where $BaFe_{12}O_{19}$ is a ferrimagnetic insulator, the topological surface states of Bi_2Se_3 remained intact and effectively generated polarized spin currents for magnetization switching, demonstrating high SOT efficiency (Fig. 5d).

Symmetry engineering

Perpendicular magnetization is highly valued in low-power high-density magnetic memory and logic devices, making deterministic switching of perpendicular magnets essential[6,137,138]. Anti-damping torque $\tau_{AD} \propto \mathbf{m} \times (\mathbf{m} \times \boldsymbol{\sigma})$ generated by spin current with polarization $\boldsymbol{\sigma}$ can switch magnetic moments effectively and deterministically when the easy axis aligns with the direction of the polarization $\boldsymbol{\sigma}$. Consequently, a perpendicular magnet can be switched deterministically via a z-polarized anti-damping torque $\boldsymbol{\tau}_{AD,z}$. Yet, most spin source materials are found to generate spin–orbit torque corresponding to y-polarization due to symmetry restrictions. Because the spin angular momentum is an axial vector (or pseudovector), a spin current with z-polarization would change its sign under mirror reflection in xz plane $\hat{M}_y : (x, y, z) \rightarrow (x, -y, z)$, which contradicts the translational symmetry present in the materials. This

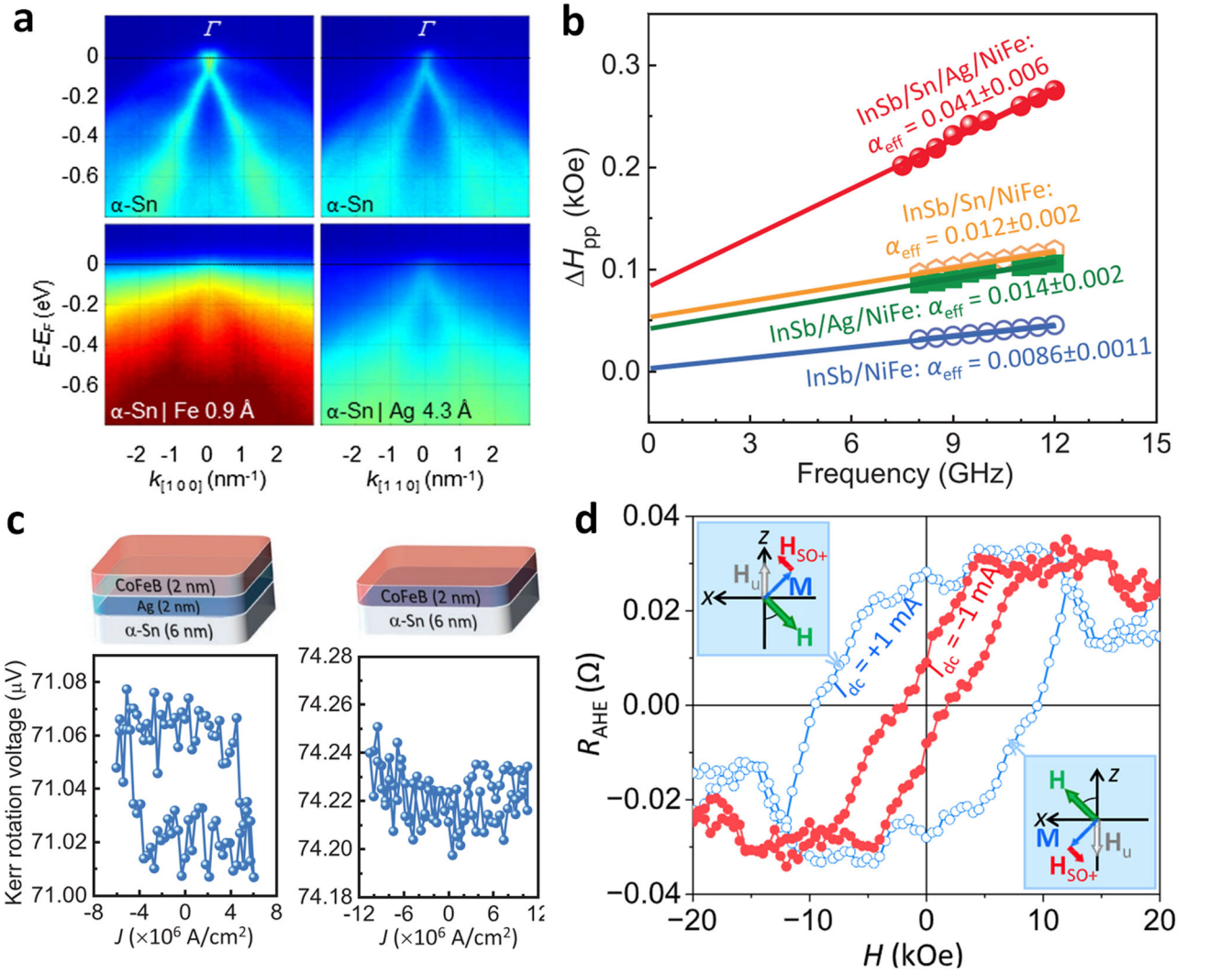

Fig. 5 | Topological surface state affected by the adjacent magnetic layer. **a** Comparison of ARPES results among α-Sn, α-Sn/Fe, and α-Sn/Ag structures[135]. **b** Comparison of magnetic damping in different structures[136]. **c** Current-induced magnetization switching via topological surface states α-Sn protected by the insertion Ag layer[86]. **d** Loop shift in $Bi_2Se_3/BaFe_{12}O_{13}$ structure with different currents[90].

restriction prohibits the generation of *z*-polarized spin current (see Fig.1c)[39,40]. An external magnetic field along the current direction is typically required to break the symmetry and facilitate the deterministic switching, which is, however, unpractical for applications.To realize the field-free deterministic switching of perpendicular magnets, various strategies of mirror symmetry breaking have been developed and can be classified into the following three categories:

(1) Asymmetric device design: This approach involves breaking mirror symmetry by introducing asymmetric design features at the device level, such as non-uniform distribution of film thickness and composition variations.

(2) Crystalline symmetry breaking: This approach involves mirror symmetry broken due to the inherently low symmetry of the lattice structure.

(3) Magnetic symmetry breaking: This approach involves mirror symmetry breaking by the introduction of long-range magnetic ordering in the spin source layer, such as a cluster magnetic octupole moment in non-collinear antiferromagnets (AFM), a Néel vector in collinear antiferromagnets, and a magnetic moment from a FM layer.

In this section, we review recent research progress on current-induced, deterministic, field-free switching of perpendicular magnetization through symmetry engineering in spin source/FM structures.

Asymmetric device design

Asymmetric device design introduces structural asymmetry at the device level to break mirror symmetry, achievable through non-uniform distributions of film thickness[39,138] and composition[139–143].

For instance, in the Ta/CoFeB/TaO_x(wedge) heterostructure[39], where the TaO_x layer has a wedge shape with a linearly changing thickness across the lateral direction (Fig. 6a), current-induced field-free switching of perpendicular magnets was observed. This switching was attributed to a new field-like effective field in the z-direction $\boldsymbol{H_z^{FL}}$, arising from the lateral thickness-gradient, which facilitated the switching of the perpendicular magnetization. Reversing the current direction to oppose the thickness gradient resulted in an opposite switching polarity, as shown in the current-induced switching measurements (Fig. 6b, c)[39]. This further demonstrated that the effective field $\boldsymbol{H_z^{FL}}$ is dependent on the thickness-gradient. A similar wedge structure in a Ta/CoFeB(wedge)/MgO multilayer also enabled field-free switching of the perpendicular magnetization (Fig. 6d)[138]. The trapezoidal shape of the edges in these structures breaks the symmetry and provide an intrinsic bias magnetic field, enabling field-free switching of perpendicular magnetization (Fig. 6e, f)[138].

In addition to lateral thickness-gradient, lateral gradient of composition in the spin source layer or magnetic layer have been also reported to break mirror symmetry and realize field-free switching of perpendicular

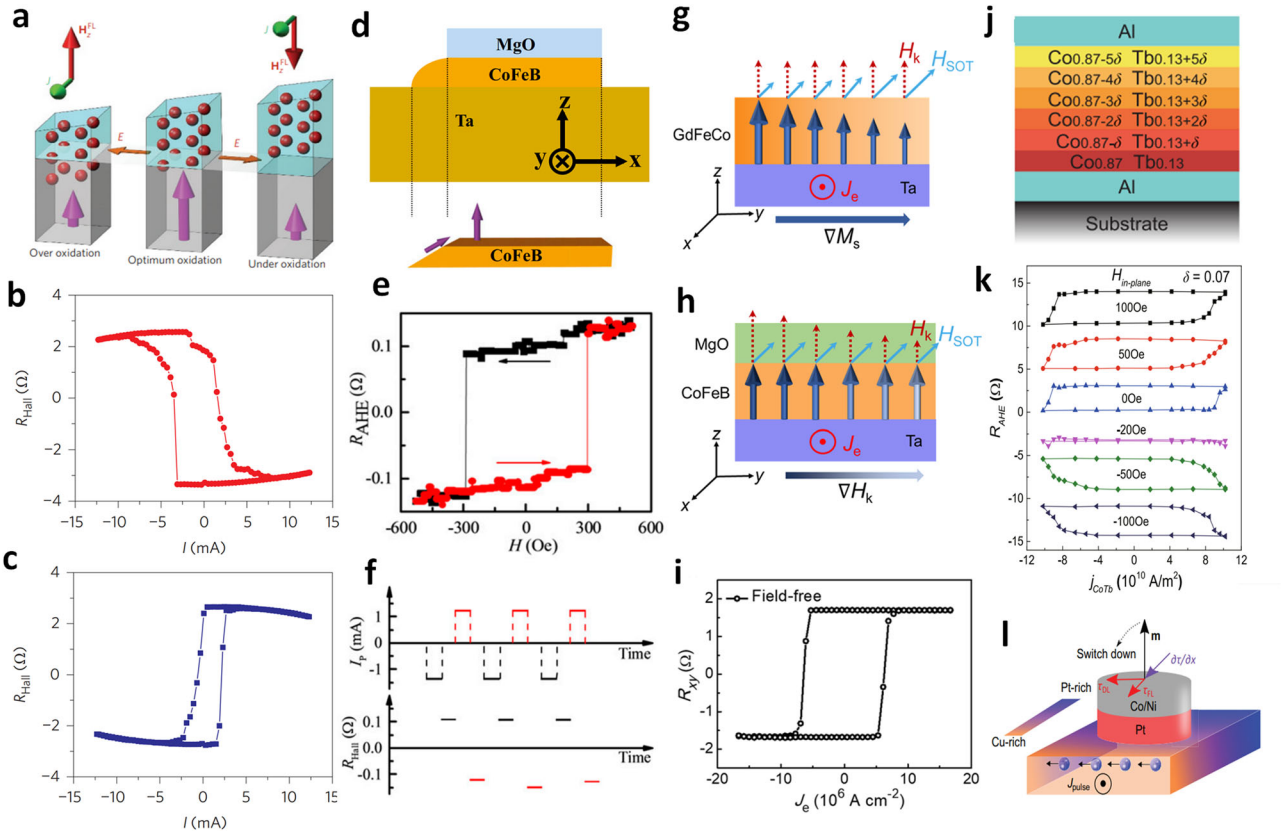

Fig. 6 | Asymmetric device design. a–c Ta/CoFeB/TaO_x(wedge)[39]: **a** Schematic of generating oop effective field H_z^{FL}. Current-induced switching with current along one (**b**) and the opposition **c** thickness-gradient direction. **d–f** Ta/CoFeB(wedge)/MgO[138]: **d** Schematic of the heterostructure. **e** Anomalous Hall resistance. **f** Current-induced switching. **g–i** Lateral magnetic gradient[142]: **g** saturation magnetization M_s or **h** magnetic anisotropy field H_k. **i** Magnetization switching with charge current. **j–k** Vertical composition gradient in Co_xTb_{1-x}[139]: **j** Schematic of vertical composition distribution of the Co_xTb_{1-x} film. **k** Current-induced perpendicular magnetization switching. **l** Cu–Pt[143]: Schematic of Cu–Pt/Pt/Co/Ni heterostructure with lateral composition gradient in Cu–Pt layer.

magnetization[140]. The lateral composition gradient in Cu–Pt spin source layer, as depicted in Fig. 6l, generated a lateral gradient of SOT and broke mirror symmetry[143]. Composition gradient in magnetic layer modulated the saturation magnetization M_s (Fig. 6g) or magnetic anisotropy field H_k (Fig. 6h), generating non-collinear spin texture with in-plane components. The Dzyaloshinskii–Moriya interaction (DMI) which broke chiral symmetry, resulted in deterministic switching without an external field (Fig. 6i).

Introduction of vertical asymmetrical structures has also been reported to contribute to field-free switching of perpendicular magnetization. In a ferrimagnetic $Co_{1-x}Tb_x$ thin film with perpendicular magnetic anisotropy(PMA), where the components of Co and Tb continuously changed in the vertical direction and formed a composition gradient (Fig. 6d)[139], researchers observed current-induced field-free switching of the perpendicular magnet in $Co_{1-x}Tb_x$ film. This was attributed to the presence of a composition gradient-driven DMI, which broke the **xz** mirror symmetry and allow generation of a **z**-polarized torque.

The advantages of using the asymmetric device design lies in its versatility; it can be applied to various types of spin source materials, including the simple heavy metals which are compatible semiconductor technology. However, adaptation of these designs for use in SOT-MTJ devices and scaling them up for industrial mass production still requires experimental demonstrations. These developments are crucial for validating the designs' compatibility and feasibility in practical applications.

Crystalline symmetry breaking

Asymmetric device design represents an "extrinsic" approach for achieving symmetry breaking. In contrast, symmetry breaking arising from the inherent material structure such as crystalline structure is "intrinsic".

Crystalline symmetry breaking can be realized in spin source materials with intrinsic low crystalline symmetry[95,144–146]. Transition-metal dichalcogenides, for example, are particular notable for their for their strong SOC and low crystalline symmetry, making them prime candidates for this approach. Significant *z*-polarized SOT has been observed in materials like tungsten ditelluride WTe_2 which possesses a layered orthorhombic structure with the space group $Pmn2_1$[144,147–150]. In a WTe_2/Py bilayer, an out-of-plane anti-damping torque with corresponding SOT efficiency of 0.016 and SOT conductivity of $(3.6 \pm 0.8) \times 10^3$ $(\hbar/2e)\ \Omega^{-1}\ cm^{-1}$ is reported (Fig. 7a–c)[144]. Besides, it is found that this unconventional torque is crystalline orientation dependent. Angle-dependent asymmetry components V_A from Lorentzian fitting of ST-FMR spectra reveals the presence of an out-of-plane anti-damping torque when charge current is in *a*-axis direction (Fig. 7b).When current is along *b*-axis with mirror symmetry the out-of-plane anti-damping torque vanishes (Fig. 7c). In addition, thickness dependence study reveales a decreased trend of this *z*-polarized SOT with increasing WTe_2 film thickness, indicating its interfacial origin in the WTe_2/FM heterostructure[147]. Field-free switching of two-dimensional(2D) PMA magnets via the *z*-polarized SOT was also demonstrated in WTe_2/PMA structure[150]. Other transition-metal dichalcogenides with similar crystalline structure as WTe_2 are also found to show SOT with *z* polarization. In $MoTe_2$/Py structure, a small out-of-plane anti-damping torque efficiency of 0.005 was reported, as well as the same crystalline-dependent trend[151]. While in $NbSe_2$, unconventional torque was not observed, which was attributed to crystalline change under strain during device processing[152] .

Apart from transition-metal dichalcogenides, recent study on ternary 2D material, Weyl semimetal $TaIrTe_4$, also reports observation of a large out-of-plane SOT with similar crystalline orientation-dependent (Fig. 7d–f)[146]. Loop shift measurement in the absence of an in-plane magnetic

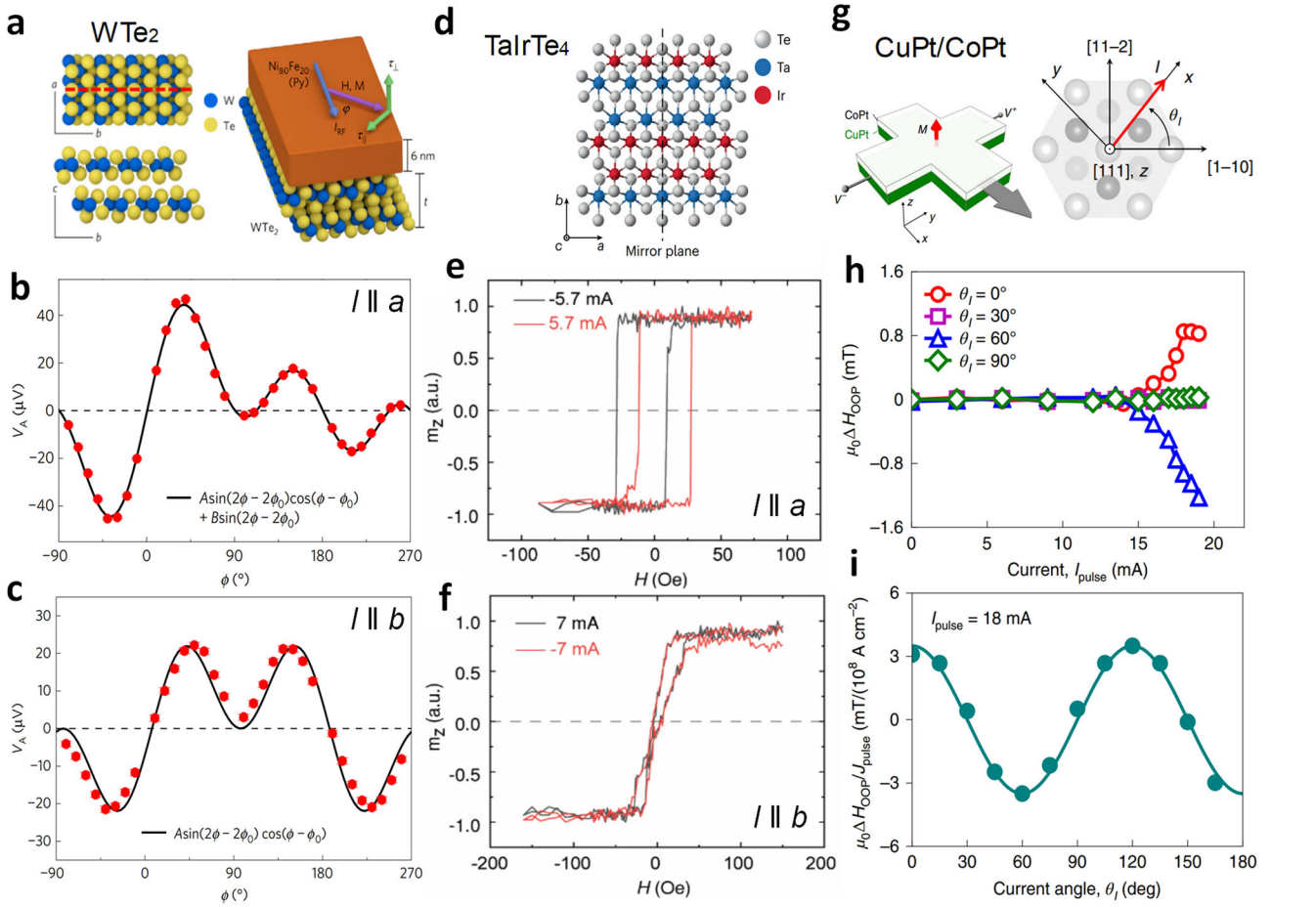

Fig. 7 | Crystalline symmetry breaking. a–c WTe_2/Py structure[144]: **a** Schematic of the crystalline structure(left) and device(right). Angle-dependent asymmetry components V_A from ST-FMR spectra when current ran (**b**) along *a*-axis (**c**) along *b*-axis. **d–f** $TaIrTe_4$/Py structure[146]: **d** Schematic of the crystalline structure. Hysteresis loop shift measurement when current ran **e** along *a*-axis (**f**) along *b*-axis. **g**, **h** CuPt/CoPt structure[96]: **g** Schematic of the device(left) and crystalline structure at the interface(right), **h** current-induced out-of-plane effective field from loop-shift measurement, and **i** crystalline orientation dependence of the out-of-plane effective field per current density.

field shows shift and an out-of-plane effective field when charge current aligns with *a*-axis (Fig. 7d). And the shift disappears in the anomalous Hall loop when current is along *b*-axis where a mirror present (Fig. 7f). The SOT efficiency of this unconventional torque is estimated to be 0.043 ± 0.003 from ST-FMR measurement, with SHC of $(2.065 \pm 0.014) \times 10^4$ $(\hbar/2e)\ \Omega^{-1}\ cm^{-1}$, which is around 1/3 of its conventional *y*-polarized SOT efficiency. The same trend of the out-of-plane anti-damping torque on the $TaIrTe_4$ thickness is also found.

In addition to 2D materials/FM bilayers, investigation on heterostructures based on CoPt have led to several interesting findings.

In the $L1_1$-ordered CuPt/CoPt heterostructure[96], the low crystallilne symmetry at the interface leads to generation of an unconventional SOT with maximum effective field of 0.03 mT per 10^6 A/cm^2 (Fig. 7g–i). Loop shfit measurements reveals that an out-of-plane effective field $\mu_0\Delta H_{OOP}$ exists when charge current is at the low crystalline symemtry direction, for instance, when the current angle θ_I is 0° or 60° (Fig. 7h). The presence of the threhold current indicats an out-of-plane anti-damping torque. More detailed experiments shows this out-of-plane effective field has a threefold rotation symmetry with respect to the current angle (Fig. 7i). The corrsponding torque is denoted as "3m" torque due to the symmetry. Similar result is also reported in single magnetic layer, an A_1-disordered $Co_{30}Pt_{70}$ alloy thin film, where the same trend of the SOT effecitve field on current direction is observed[95]. In this case, the presence of the SOT and the free-field switching of the same layer is attributed to the cooperation of two structural mechanisms: the low crystal symmetry at the Co platelets/Pt interfaces which gave rise to the "3 *m*" torque, and the composition gradient along the thickness direction which broke the mirror symmetry along the *z*-plane. However, in another study a field-like torque corresponding to the x-polarization instead of z-polariztion is reported in a $[Pt/Co]_5$/CoFeB multilayer, where the Co films is ultrathin ($t < 0.260$ nm) and presents paramagnetic state[153]. In this structure, symmetry breaking is considered to be obtained through a weak in-plane magnetization of Co, acquired from the stray field of the adjacent in-plane magnetized CoFeB film via magnetic proximity effect.

In brief, out-of-plane SOTs can be generated from a spin source layer with low crystalline symmetry and with mirror symemmtry breaking. The magnitude of the out-of-plane SOTs hence depend strongly on the crystalline orientation.

Magnetic symmetry breaking

Magnetic ordering in magnetic SOT materials offers an alternative "intrinsic" approach to break mirror symmetry. The presence of long-range magnetic ordering has been proven to effectively break mirror symmetry and lead to generation of unconventional SOTs. For instance, investigation on non-collinear AFM materials reports the presence of unconventional SOT due to the presence of chiral spin texture in real space and its resulting band splitting in k-space, which is denoted as the magnetic spin Hall effect (MSHE)[82,100,154–156]. These non-collinear AFM materials include Mn_3GaN, Mn_3SnN, Mn_3Sn, Mn_3Ga, $MnPd_3$, and so on.

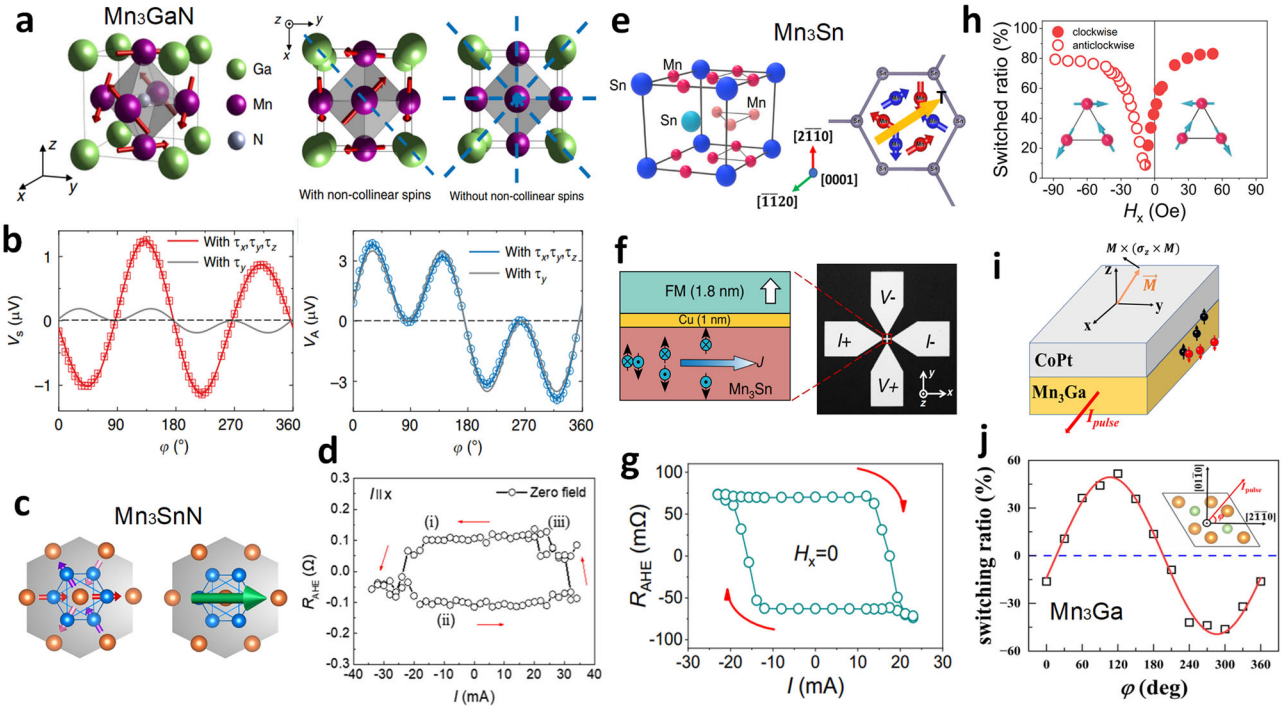

Fig. 8 | Magnetic symmetry breaking on non-collinear AFM materials. **a**, **b** Mn_3GaN structure[154]: **a** Anti-perovskite crystalline structure and the non-collinear spins(left), the (001) projection with (middle) and without (right) non-collinear spins. **b** Symmetry and asymmetry component from ST-FMR spectra indicating the presence of unconventional SOTs when current run along [100] direction. **c**, **d** Mn_3SnN structure[156]: **c** spin texture(left) and the cluster magnetic octupole moment **T**. **d** field-free switching of PMA via an out-of-plane torque. **e**–**h** Mn_3Sn structure[100]: **e** Crystalline structure(left) and the cluster magnetic octupole moment **T**(right) along the (0001) direction. **f** Schematic of the device. **g** Field-free switching of PMA via *z*-polarized torques and **h** switching polar(-clockwise or anticlockwise) reversed with changing spin texture. **i**, **j** Mn_3Ga structure[145]: **i** Schematic of the device and **j** crystalline orientation-dependent switching ratio on the (0001) plane.

Table 1 | Comparison of SHA of different spin source materials with symmetry breaking *t*

Materials	ρ ($\mu\Omega$cm)	θ_z	θ_y	θ_z/θ_y	Methods	Temperature	References
WTe_2	380	0.013	0.03	43%	ST-FMR	300 K	144
$TaIrTe_4$	80	0.043	0.113	38%	ST-FMR	300 K	146
Mn_3GaN	220	0.019	0.025	76%	ST-FMR	300 K	154
Mn_3Sn	367	0.067	0.22	31%	Loop-shift	300 K	159
$MnPd_3$	60	0.011	0.41	2.7%	SHH	4 K	155

Mn_3GaN is a metallic manganese nitride of anti-perovskite crystalline structure, and belongs to the space group $Pm\bar{3}m$. The spins of the Mn atoms form Kagome structure in the (111) plane due to magnetic frustration, reducing the mirror planes to only one in (110) (Fig. 8a)[157,158]. Unconventional torques corresponding to z-polarization and x-polarization were reported by ST-FMR measurement (Fig. 8b)[154]. Temperature dependent ST-FMR study shows that these unconventional torque vanish when the sample temperature is larger than the Néel temperature of Mn_3GaN, confirming the important role of the magnetic structure in generating unconventional torques. Out-of-plane SOT also is also found in Mn_3SnN thin film with the similar crystalline and magnetic structure (Fig. 8c)[156], and field-free switching of perpendicular magnetization is also demonstrated (Fig. 8d).

Mn_3Sn is hexagonal structure belonging to the $P6_3/mmc$ space group and a non-collinear AFM with Kagome plane on the (0001) plane (Fig. 8e). Out-of-plane and conventional anti-damping torques were reported in the Mn_3Sn/Cu/FM structure (Fig. 8f)[100]. In loopshift measurement where charge current was in the Kagome plane and aligns with the cluster magnetic octupole moment T, the corresponding SHA of out-of-plane torque and conventional torque were evaluted to be 0.067 and 0.22, respectively. Field-free switching in the Mn_3Sn/Cu/PMA structure showed efficiency switching at 20 mA with critical current density of 5×10^6 A/cm^2 (Fig. 8g). The switching polarity(clockwise or anticlockwise) and switching ratio is not symemtric with respect to the magnetic fields due to a preferred AFM domain orientation in Mn_3Sn during the deposition process (Fig. 8h). And in the field-free switching experiment in the Mn_3Ga(0001)/PtCo heterostructure[145], the switching polarity and switching ratio present a sinusoidal relation with respect to the current direction (Fig. 8i, j). It is also worth mentioned that when the non-collinear AFM works as a detected layer instead of a spin source layer, the octupole moment in the Mn_3Sn layer rotates in an opposite direction with the individual moments under SOT switching, resulting in a distinct SOT switching polarity from ferromagnets[159].

A summary of electric resistivity, SHA of the out-of-plane torque θ_z, SHA of the conventional torque θy, the ratio $\theta z/\theta y$ of spin source materials with intrinsic symmetry breaking is listed in Table 1.

The generation of an in-plane component of magnetization or effective magnetic field is another way for magnetic symmetry breaking. In PtMn/CoNi structure, where Néel vector of the AFM film PtMn is lying in-plane, investigation showed that deterministic switching of the perpendicular magnetization in CoNi via current-induced spin–orbit torque was realized without the aid of an external magnetic field (Fig. 9a–c)[160]. Because the spins

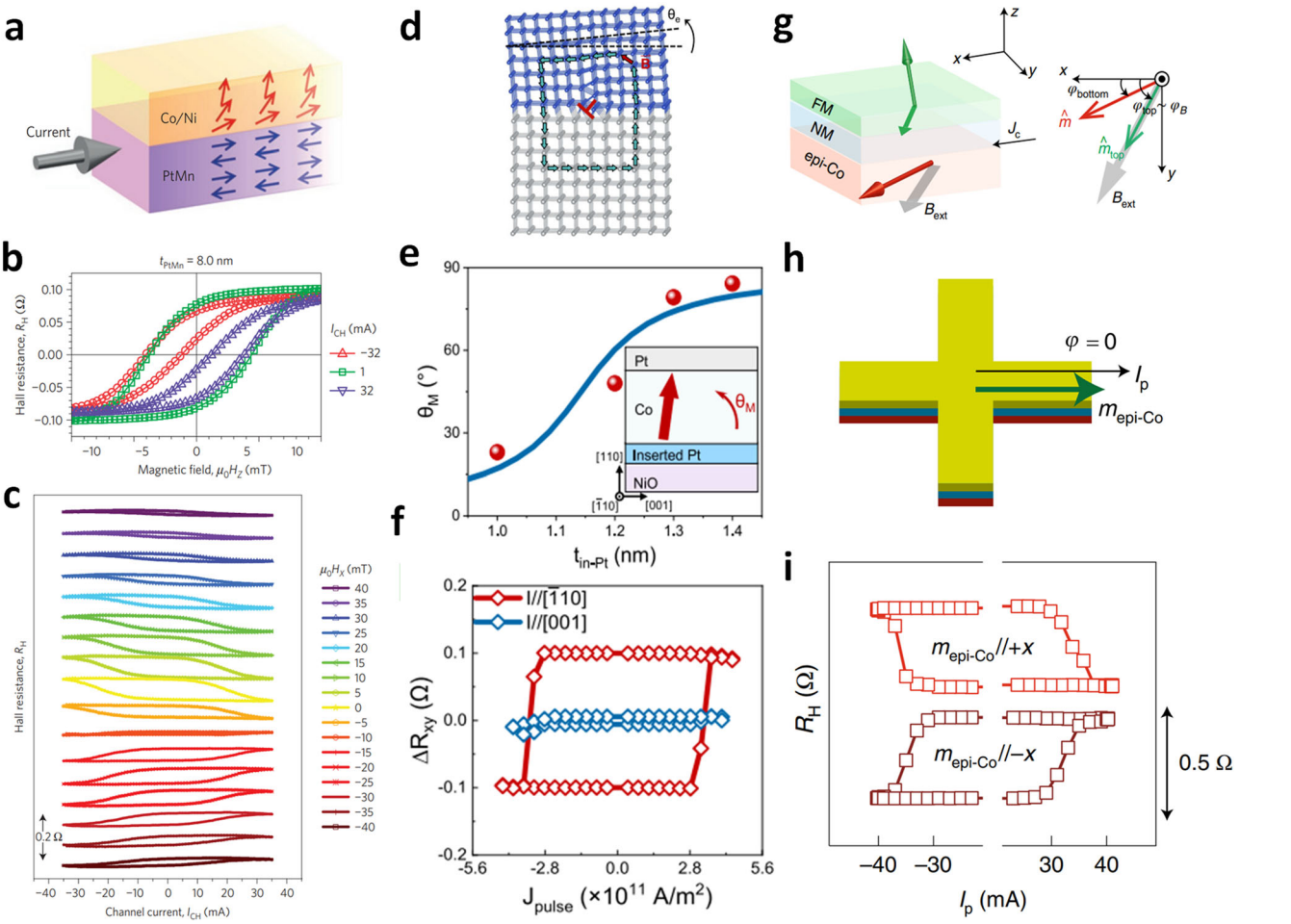

Fig. 9 | Symmetry breaking via generation of an in-plane effective field or magnetization. Mirror symmetry breaking via (**a**–**c**) AFM-FM exchange field in PtMn/CoNi structure[160]: **a** Schematic of the spin orientation, **b** Hall resistance showing the presence of an exchange field, and **c** current-induced magnetization switching. **d**–**f** Tilted magnetic moment in Pt/Co/Pt/NiO structure[98]: **d** Schematic of the dislocation leading to tilted crystalline planes. **e** The tilted magnetic moment varied with the thickness of insertion Pt layer and **f** current-induced magnetization switching. **g**–**i** In-plane magnetic moment with strong IMA in Co(epi)/NM/FM structure[165]: **g** Schematic of the trilayer. **h** Schematic of the Hall bar measurement setup with magnetic moment of Co(epi) lying in the current direction and **i** current-induced field-free magnetization switching.

in ferromagnetic CoNi layer near the interface were pinned at the Néel vector direction due to exchange coupling, an in-plane exchange field appeared and broke the mirror symmetry, allowing generation of out-of-plane SOTs. In other AFM/FM systems, such field-free switching of perpendicular magnets were also demonstrated, such as in the IrMn/CoFeB[161], PtMn/CoFeB[162] stack structures.

A tilted magnetic moment is also an effective approach to offer in-plane symmetry breaking. In an epitaxial grown Pt/Co heterostructure, dislocations generates crystal lattice tilting with respect to the substrate plane, leading to a tilted magnetic easy axis deviated from the perpendicular direction (Fig. 9d)[98]. The in-plane component of this tilted magnetic moment breaks the mirror symmetry (Fig. 9e). And field-free switching of the tilted magnetic moment in Pt/Co heterostructure was also demonstrated (Fig. 9f). Tilted magnetic anisotropy axis and field-free switching is also achieved in ferrimagnetic Gd/Co multilayers[163]. In an epitaxial collinear antiferromagnetic ruthenium dioxide RuO_2(101) film, where the Néel vector in [001] direction was tilted relative the sample plane, an out-of-plane anti-damping torque was also found via ST-FMR measurement[164].

An in-plane magnetic moment from an extra magnetic layer could also help to break mirror symmetry. In epitaxial-Co/HM/FM trilayers (Fig. 9g)[165], it is reported that the large in-plane magnetocrystalline anisotropy(IMA) in epitaxial Co film ensures a magnetic moment component in the current direction ($m_{epi\text{-}Co} \parallel x$) (Fig. 9h), which breaks the mirror symmetry and leads to field-free switching of perpendicular magnetization (Fig. 9i).

Summary and outlooks

Optimizing spin source materials through material design is a promising pathway toward power-efficient spintronic application. This includes strain engineering, interface engineering and symmetry engineering. Strain engineering has led to enhanced SOT efficiency in complex oxides, heavy metals and alloys. Interface engineering led to protected topological surface states and improved spin transparency. Symmetry engineering enabled deterministic, field-free switching of perpendicular magnets via symmetry breaking approaches, such as asymmetric device design, crystalline symmetry breaking and magnetic symmetry breaking.

Despite these advancements, significant challenges remain in fully harnessing the potential of SOTs through material design: (1) Strain Engineering: A comprehensive understanding of how crystalline structure influences electronic properties and spin-Hall conductivity, especially in complex oxides, is still lacking. This is important for the design of artificial materials optimized for maximized spin-orbit torque (SOT) efficiency. Addressing this gap requires a multidisciplinary approach involving theoretical studies, advanced materials characterization techniques, and artifact-free spin torque measurements. Furthermore, the development of new

experimental methods capable of applying larger and more tunable strains to single-crystalline SOT materials is crucial. Innovations such as free-standing single crystalline films on flexible substrates could enable more profound modulation of the strain effects on SOT, leading to significant enhancements in SOT efficiency. (2) Interface Engineering: The mechanisms by which the insertion of antiferromagnetic oxide layers at interfaces enhances spin transparency remain ambiguous, particularly regarding the potential roles of magnon-mediated currents, which is still a subject of active debate. Despite these uncertainties, integrating antiferromagnetic or multiferroic materials at the interface provides substantial benefits. These materials introduce additional functionalities and enable voltage tunability in spin-orbitronic devices, offering new ways to manipulate spin currents and magnetic states effectively. (3) Symmetry Engineering: The precision required in asymmetric device design and the handling of materials with low crystalline symmetry or long-range magnetic ordering pose significant challenges, particularly in terms of scalability and manufacturing consistency. Addressing these issues is crucial for the transition from laboratory settings to industrial-scale production.

In conclusion, while the field of spintronics has seen considerable progress due to innovative material engineering strategies, ongoing research is essential to address the remaining technical challenges. Future work will need to focus on refining these engineering approaches and developing new methodologies to fully realize the potential of spin-orbitronics devices for next-generation beyond-CMOS technologies.

Data availability

No datasets were generated or analysed during the current study.

Received: 17 March 2024; Accepted: 7 August 2024;
Published online: 21 November 2024

References

1. Dieny, B. et al. Opportunities and challenges for spintronics in the microelectronics industry. *Nat. Electron.* **3,** 446–459 (2020).
2. Barman, A. et al. The 2021 magnonics roadmap. *J. Phys. Condens. Matter* **33**, 413001 (2021).
3. Vedmedenko, E. Y. et al. The 2020 magnetism roadmap. *J. Phys. D Appl. Phys.* **53**, 453001 (2020).
4. Sander, D. et al. The 2017 magnetism roadmap. *J. Phys. D Appl. Phys.* **50**, 363001 (2017).
5. Lu, A. et al. High-speed emerging memories for AI hardware accelerators. *Nat. Rev. Electr. Eng.* **1**, 24–34 (2024).
6. Shao, Q. et al. Roadmap of spin–orbit torques. *IEEE Trans. Magn.* **57**, 1–39 (2021).
7. Puebla, J. et al. Spintronic devices for energy-efficient data storage and energy harvesting. *Commun. Mater.* **1**, 24 (2020).
8. Khan, M. A. et al. Magnetic sensors—a review and recent technologies. *Eng. Res. Express* **3**, 022005 (2021).
9. El-Ghazaly, A. et al. Progress towards ultrafast spintronics applications. *J. Magn. Magn. Mater.* **502**, 166478 (2020).
10. Hirohata, A. et al. Review on spintronics: principles and device applications. *J. Magn. Magn. Mater.* **509**, 166711 (2020).
11. Chiu, Y.-C. et al. A CMOS-integrated spintronic compute-in-memory macro for secure AI edge devices. *Nat. Electron.* **6**, 534–543 (2023).
12. Jung, S. et al. A crossbar array of magnetoresistive memory devices for in-memory computing. *Nature* **601**, 211–216 (2022).
13. Yang, H. et al. Two-dimensional materials prospect for non-volatile spintronic memories. *Nature* **606**, 663–673 (2022).
14. Grimaldi, E. et al. Single-shot dynamics of spin–orbit torque and spin transfer torque switching in three-terminal magnetic tunnel junctions. *Nat. Nanotechnol.* **15**, 111–117 (2020).
15. Endoh, T. et al. Recent progresses in STT-MRAM and SOT-MRAM for next generation MRAM. In *2020 IEEE Symposium on VLSI Technology* (IEEE, 2020).
16. Gupta, M. et al. High-density SOT-MRAM technology and design specifications for the embedded domain at 5nm node. In *2020 IEEE International Electron Devices Meeting (IEDM)* (IEEE, 2020).
17. Liu, Y. & Yu, G. MRAM gets closer to the core. *Nat. Electron.* **2**, 555–556 (2019).
18. Hirohata, A. MRAM makes its mark. *Nat. Electron.* **5**, 832–833 (2022).
19. Demidov, V. E. et al. Synchronization of spin Hall nano-oscillators to external microwave signals. *Nat. Commun.* **5**, 3179 (2014).
20. Awad, A. A. et al. Long-range mutual synchronization of spin Hall nano-oscillators. *Nat. Phys.* **13**, 292–299 (2017).
21. Torrejon, J. et al. Neuromorphic computing with nanoscale spintronic oscillators. *Nature* **547**, 428–431 (2017).
22. Dutta, S. et al. An Ising Hamiltonian solver based on coupled stochastic phase-transition nano-oscillators. *Nat. Electron.* **4**, 502–512 (2021).
23. Choi, J. G. et al. Voltage-driven gigahertz frequency tuning of spin Hall nano-oscillators. *Nat. Commun.* **13**, 3783 (2022).
24. Haidar, M. et al. A single layer spin-orbit torque nano-oscillator. *Nat. Commun.* **10**, 2362 (2019).
25. Zahedinejad, M. et al. Memristive control of mutual spin Hall nano-oscillator synchronization for neuromorphic computing. *Nat. Mater.* **21**, 81–87 (2022).
26. Grollier, J. et al. Neuromorphic spintronics. *Nat. Electron.* **3**, 360–370 (2020).
27. Sangwan, V. K. & Hersam, M. C. Neuromorphic nanoelectronic materials. *Nat. Nanotechnol.* **15**, 517–528 (2020).
28. Zhou, J. & Chen, J. Prospect of spintronics in neuromorphic computing. *Adv. Electron. Mater.* **7**, 2100465 (2021).
29. Kumar, D. et al. Ultralow energy domain wall device for spin-based neuromorphic computing. *ACS Nano* **17**, 6261–6274 (2023).
30. Yang, Q. et al. Spintronic integrate-fire-reset neuron with stochasticity for neuromorphic computing. *Nano Lett.* **22**, 8437–8444 (2022).
31. Zhang, S. et al. Nanoscale vector magnetic sensing with current-driven stochastic nanomagnet. *Adv. Electron. Mater.* 10, 2300753 (2024).
32. Li, R. et al. A spin–orbit torque device for sensing three-dimensional magnetic fields. *Nat. Electron.* **4**, 179–184 (2021).
33. Qin, Y. et al. Magnetic anomaly detection using full magnetic gradient orthonormal basis function. *IEEE Sens. J.* **20**, 12928–12940 (2020).
34. Ma, Z.-L. et al. Developing highly sensitive SAW standing wave magnetic sensor through resonant frequency shift and acoustic energy concentration. *IEEE Sens. J.* (2024).
35. Edelstein, D. et al. A 14 nm embedded STT-MRAM CMOS technology. In *2020 IEEE International Electron Devices Meeting (IEDM)* (IEEE, 2020).
36. Ikegawa, S. et al. Magnetoresistive random access memory: present and future. *IEEE Trans. Electron Devices* **67**, 1407–1419 (2020).
37. Khvalkovskiy, A. V. et al. Basic principles of STT-MRAM cell operation in memory arrays. *J. Phys. D Appl. Phys.* **46**, 074001 (2013).
38. Liu, L. et al. Spin-torque switching with the giant spin Hall effect of tantalum. *Science* **336**, 555–558 (2012).
39. Yu, G. et al. Switching of perpendicular magnetization by spin–orbit torques in the absence of external magnetic fields. *Nat. Nanotechnol.* **9**, 548–554 (2014).
40. Bhowmik, D., You, L. & Salahuddin, S. Spin Hall effect clocking of nanomagnetic logic without a magnetic field. *Nat. Nanotechnol.* **9**, 59–63 (2014).
41. Kent, A. & Worledge, D. A new spin on magnetic memories. *Nat. Nanotechnol.* **10**, 187–191 (2015).
42. Sinova, J. et al. Spin Hall effects. *Rev. Mod. Phys.* **87**, 1213 (2015).
43. Jungwirth, T., Wunderlich, J. & Olejník, K. Spin Hall effect devices. *Nat. Mater.* **11**, 382–390 (2012).

44. Safranski, C., Eric, A. M. & Ilya, N. K. Spin–orbit torque driven by a planar Hall current. *Nat. Nanotechnol.* **14**, 27–30 (2019).
45. Kondou, K. et al. Giant field-like torque by the out-of-plane magnetic spin Hall effect in a topological antiferromagnet. *Nat. Commun*. **12**, 6491 (2021).
46. Hai, P. N. Spin Hall effect in topological insulators. *J. Magn. Soc. Jpn.* **44**, 137–144 (2020).
47. Mihai Miron, I. et al. Current-driven spin torque induced by the Rashba effect in a ferromagnetic metal layer. *Nat. Mater.* **9**, 230 (2010).
48. Manchon, A., Koo, H. C., Nitta, C. J., Frolov, S. M. & Duine, R. A. New perspectives for Rashba spin–orbit coupling. *Nat. Mater.* **14**, 871 (2015).
49. Bihlmayer, G. et al. Rashba-like physics in condensed matter. *Nat. Rev. Phys.* **4**, 642–659 (2022).
50. Koo, H. C. et al. Rashba effect in functional spintronic devices. *Adv. Mater.* **32**, 2002117 (2020).
51. Song, Q. et al. Observation of inverse Edelstein effect in Rashba-split 2DEG between $SrTiO_3$ and $LaAlO_3$ at room temperature. *Sci. Adv.* **3**, e1602312 (2017).
52. Sunko, V. et al. Maximal Rashba-like spin splitting via kinetic-energy-coupled inversion-symmetry breaking. *Nature* **549**, 492–496 (2017).
53. El Hamdi, A. et al. Observation of the orbital inverse Rashba–Edelstein effect. *Nat. Phys.* **19**, 1855–1860 (2023).
54. Kontani, H., Tanaka, T., Hirashima, D. S., Yamada, K. & Inoue, J. Giant orbital Hall effect in transition metals: origin of large spin and anomalous Hall effects. *Phys. Rev. Lett.* **102**, 1660 (2009).
55. Choi, Y.-G. et al. Observation of the orbital Hall effect in a light metal Ti. *Nature* **619**, 52–56 (2023).
56. Chen, X. et al. Giant antidamping orbital torque originating from the orbital Rashba-Edelstein effect in ferromagnetic heterostructures. *Nat. Commun.* **9**, 2569 (2018).
57. Lyalin, I. et al. Magneto-optical detection of the orbital Hall effect in chromium. *Phys. Rev. Lett.* **131**, 156702 (2023).
58. Huang, Q. et al. Current-induced magnetization switching in light-metal-oxide/ferromagnetic-metal bilayers via orbital Rashba effect. *Nano Lett.* **23**, 11323–11329 (2023).
59. Onose, Y. et al. Observation of the magnon Hall effect. *Science* **329**, 297–299 (2010).
60. Zhitomirsky, M. E. & Chernyshev, A. L. Colloquium: spontaneous magnon decays. *Rev. Mod. Phys.* **85**, 219 (2013).
61. Andrii, V. et al. Magnon spintronics. *Nat. Phys.* **11**, 453–461 (2015).
62. Wang, Y. et al. Magnetization switching by magnon-mediated spin torque through an antiferromagnetic insulator. *Science* **366**, 1125 (2019).
63. Andrii, V. et al. Advances in magnetics roadmap on spin-wave computing. *IEEE Trans. Magn.* **58**, 1–72 (2022). Chumak.
64. Li, R. et al. A puzzling insensitivity of magnon spin diffusion to the presence of 180-degree domain walls. *Nat. Commun.* **14**, 2393 (2023).
65. Chai, Y. et al. Voltage control of multiferroic magnon torque for reconfigurable logic-in-memory. *Nat. Commun*. **15**, 5975 (2024).
66. McCullian, B. A. et al. Broadband multi-magnon relaxometry using a quantum spin sensor for high frequency ferromagnetic dynamics sensing. *Nat. Commun.* **11**, 5229 (2020).
67. Lifshits, M. B. & Dyakonov, M. I. Swapping spin currents: interchanging spin and flow directions. *Phys. Rev. Lett.* **103**, 186601 (2009).
68. Saidaoui, H. B. M. & Manchon, A. Spin-swapping transport and torques in ultrathin magnetic bilayers. *Phys. Rev. Lett.* **117**, 036601 (2016).
69. Lin, W. et al. Evidence for spin swapping in an antiferromagnet. *Nat. Phys.* **18**, 800–805 (2022).
70. Hazra, B. K. et al. Generation of out-of-plane polarized spin current by spin swapping. *Nat. Commun.* **14**, 4549 (2023).
71. Zhu, L., Ralph, D. C. & Buhrman, R. A. Effective spin-mixing conductance of heavy-metal–ferromagnet interfaces. *Phys. Rev. Lett.* **123**, 057203 (2019).
72. Zhu, L. et al. Variation of the giant intrinsic spin Hall conductivity of Pt with carrier lifetime. *Sci. Adv.* **5**, eaav8025 (2019).
73. Zhu, L., Ralph, D. C. & Buhrman, R. A. Enhancement of spin transparency by interfacial alloying. *Phys. Rev. B* **99**, 180404 (2019).
74. Prenat, G. et al. Beyond STT-MRAM, spin orbit torque RAM SOT-MRAM for high speed and high reliability applications. *Spintronics-based Comput.* 145–157 (2015).
75. Kim, S. K. et al. Ferrimagnetic spintronics. *Nat. Mater.* **21**, 24–34 (2022).
76. Ding, J. et al. Nanometer-thick yttrium iron garnet films with perpendicular anisotropy and low damping. *Phys. Rev. Appl.* **14**, 014017 (2020).
77. Li, P. et al. Spin–orbit torque-assisted switching in magnetic insulator thin films with perpendicular magnetic anisotropy. *Nat. Commun.* **7**, 12688 (2016).
78. Yu, J. et al. Long spin coherence length and bulk-like spin–orbit torque in ferrimagnetic multilayers. *Nat. Mater.* **18**, 29–34 (2019).
79. Fukami, S. et al. Magnetization switching by spin–orbit torque in an antiferromagnet–ferromagnet bilayer system. *Nat. Mater.* **15**, 535–541 (2016).
80. Godinho, J. et al. Electrically induced and detected Néel vector reversal in a collinear antiferromagnet. *Nat. Commun.* **9**, 4686 (2018).
81. Chiang, C. C. et al. Absence of evidence of electrical switching of the antiferromagnetic Néel vector. *Phys. Rev. Lett.* **123**, 227203 (2019).
82. Chen, X. et al. Observation of the antiferromagnetic spin Hall effect. *Nat. Mater.* **20**, 800–804 (2021).
83. Chen, H. & Di, Y. Spin–charge conversion in transition metal oxides. *APL Mater.* **9**, 6 (2021).
84. Nan, T. et al. Anisotropic spin-orbit torque generation in epitaxial $SrIrO_3$ by symmetry design. *Proc. Natl. Acad. Sci. USA* **116**, 16186 (2019).
85. Shi, S. et al. All-electric magnetization switching and Dzyaloshinskii–Moriya interaction in WTe2/ferromagnet heterostructures. *Nat. Nanotechnol.* **14**, 945–949 (2019).
86. Ding, J. et al. Switching of a magnet by spin-orbit torque from a topological Dirac semimetal. *Adv. Mater.* **33**, 2005909 (2021).
87. Fan, Y. et al. Electric-field control of spin–orbit torque in a magnetically doped topological insulator. *Nat. Nanotechnol.* **11**, 352–359 (2016).
88. Han, J. et al. Room-temperature spin-orbit torque switching induced by a topological insulator. *Phys. Rev. Lett.* **119**, 077702 (2017).
89. Wang, Y. et al. Room temperature magnetization switching in topological insulator-ferromagnet heterostructures by spin-orbit torques. *Nat. Commun.* **8**, 1364 (2017).
90. Li, P. et al. Magnetization switching using topological surface states. *Sci. Adv.* **5**, eaaw3415 (2019).
91. Wu, H. et al. Magnetic memory driven by topological insulators. *Nat. Commun.* **12**, 6251 (2021).
92. Dc, M. et al. Room-temperature high spin–orbit torque due to quantum confinement in sputtered Bi x Se (1–x) films. *Nat. Mater.* **17**, 800–807 (2018).
93. Jeongchun, R. et al. Current-induced spin–orbit torques for spintronic applications. *Adv. Mater.* **32**, 1907148 (2020).
94. Yang, Q. et al. Field-free spin–orbit torque switching in ferromagnetic trilayers at sub-ns timescales. *Nat. Commun.* **15**, 1814 (2024).
95. Liu, L. et al. Current-induced self-switching of perpendicular magnetization in CoPt single layer. *Nat. Commun.* **13**, 3539 (2022).
96. Liu, L. et al. Symmetry-dependent field-free switching of perpendicular magnetization. *Nat. Nanotechnol.* **16**, 277–282 (2021).

97. Xie, X. et al. Controllable field-free switching of perpendicular magnetization through bulk spin-orbit torque in symmetry-broken ferromagnetic films. *Nat. Commun.* **12**, 2473 (2021).
98. Liang, Y. et al. Field-free spin-orbit switching of perpendicular magnetization enabled by dislocation-induced in-plane symmetry breaking. *Nat. Commun.* **14**, 5458 (2023).
99. Chen, L. et al. Engineering symmetry breaking enables efficient bulk spin-orbit torque-driven perpendicular magnetization switching. *Adv. Funct. Mater.* **34**, 2308823 (2024).
100. Hu, S. et al. Efficient perpendicular magnetization switching by a magnetic spin Hall effect in a noncollinear antiferromagnet. *Nat. Commun.* **13**, 4447 (2022).
101. Thomas, O. et al. Interplay between anisotropic strain relaxation and uniaxial interface magnetic anisotropy in epitaxial Fe films on (001) GaAs. *Phys. Rev. Lett.* **90**, 017205 (2003).
102. Huang, W. et al. Strain induced magnetic anisotropy in highly epitaxial $CoFe_2O_4$ thin films. *Appl. Phys. Lett.* **89**, 262506 (2006).
103. Herklotz, A. et al. Designing magnetic anisotropy through strain doping. *Adv. Sci.* **5**, 1800356 (2018).
104. Zhang, Y. et al. Effects of growth order on perpendicular magnetic anisotropy of heavy-metal/ferromagnet/MgO trilayered structures. *IEEE Magn. Lett.* **10**, 1–4 (2019).
105. Ahn, G. H. et al. Strain-engineered growth of two-dimensional materials. *Nat. Commun.* **8**, 608 (2017).
106. Panasci, S. E. et al. Strain, doping, and electronic transport of large area monolayer MoS_2 exfoliated on gold and transferred to an insulating substrate. *ACS Appl. Mater. Interfaces* **13**, 31248–31259 (2021).
107. Kumar, P. & Chand, P. Structural, electric transport response and electro-strain-polarization effect in La and Ni modified bismuth ferrite nanostructures. *J. Alloy. Compd.* **748**, 504–514 (2018).
108. Frisenda, R. et al. Biaxial strain tuning of the optical properties of single-layer transition metal dichalcogenides. *NPJ 2D Mater. Appl.* **1**, 10 (2017).
109. Xiao, D., Chang, M. C. & Niu, Q. Berry phase effects on electronic properties. *Rev. Mod. Phys.* **82**, 1959–2007 (2010).
110. Guo, G. Y., Yao, Y. & Niu, Q. Ab initio calculation of the intrinsic spin Hall effect in semiconductors. *Phys. Rev. Lett.* 94, 226601 (2005).
111. Witczak-Krempa, W., Chen, G., Kim, Y. B. & Balents, L. Correlated quantum phenomena in the strong spin-orbit regime. *Annu. Rev. Condens. Matter Phys.* **5**, 57–82 (2014).
112. Dhanaraj, G., Byrappa, K., Prasad, V. & Dudley, M. (eds) *Springer Handbook of Crystal Growth* (Springer-Verlag Berlin Heidelberg, 2010).
113. Tan, C. et al. Epitaxial growth of hybrid nanostructures. *Nat. Rev. Mater.* **3**, 17089 (2018).
114. Ji, G. P. et al. Panoramic view of particle morphology for growth mechanism exploration: A case study of micron-sized five-fold twinned Ag particles from vapor condensation. *J. Cryst. Growth* **533**, 125459 (2020).
115. Zheleva, T., Jagannadham, K. & Narayan, J. Epitaxial growth in large-lattice-mismatch systems. *J. Appl. Phys.* **75**, 860–871 (1994).
116. Zhou, J. et al. Modulation of spin–orbit torque from $SrRuO_3$ by epitaxial-strain-induced octahedral rotation. *Adv. Mater.* **33**, 1 (2021).
117. Huang, X. et al. Novel spin–orbit torque generation at room temperature in an all-oxide epitaxial $La_{0.7}Sr_{0.3}MnO_3/SrIrO_3$ system. *Adv. Mater.* **33**, 2008269 (2021).
118. Li, S. et al. Room temperature spin-orbit torque efficiency and magnetization switching in $SrRuO_3$-based heterostructures. *Phys. Rev. Mater.* **7**, 024418 (2023).
119. Wei, J. et al. Enhancement of spin–orbit torque by strain engineering in $SrRuO_3$ films. *Adv. Funct. Mater.* **1**, 2100380 (2021).
120. Kim, Y. et al. Orbital and spin magnetic moments in strain-relaxed $SrRuO_3(111)/SrTiO_3$ thin films. *J. Korean Phys. Soc.* **83**, 296–300 (2023).
121. Jiang, D. et al. Substrate-induced spin-torque-like signal in spin-torque ferromagnetic resonance measurement. *Phys. Rev. Appl.* **21**, 024021 (2024).
122. Zhang, Y. et al. Strain engineering of magnetic proximity effect and spin-orbit torque in heavy metal/ferromagnet heterostructures. *J. Magn. Magn. Mater.* **498**, 166112 (2020).
123. Zhang, X. et al. Size-dependent tensile failure of epitaxial TiN/Cu/TiN sandwich pillar structures: a combined experimentation—atomistic simulation study. *Mater. Sci. Eng. R. Rep.* **855**, 143889 (2022).
124. Nan, T. et al. A strain-mediated magnetoelectric-spin-torque hybrid structure. *Adv. Funct. Mater.* **29**, 1 (2019).
125. Hwee, W. et al. Strain-mediated spin–orbit torque enhancement in Pt/Co on flexible substrate. *ACS Nano* **15**, 8319–8327 (2021).
126. Filianina, M. et al. Electric-field control of spin-orbit torques in perpendicularly magnetized W/CoFeB/MgO films. *Phys. Rev. Lett.* **124**, 217701 (2020).
127. Tokaç, M. et al. Interfacial structure dependent spin mixing conductance in cobalt thin films. *Phys. Rev. Lett.* **115**, 056601 (2015).
128. Pai, C.-F. et al. Dependence of the efficiency of spin Hall torque on the transparency of Pt/ferromagnetic layer interfaces. *Phys. Rev. B* **92**, 064426 (2015).
129. Demasius, K. U. et al. Enhanced spin–orbit torques by oxygen incorporation in tungsten films. *Nat. Commun.* **7**, 1–7 (2016).
130. Kageyama, Y. et al. Spin-orbit torque manipulated by fine-tuning of oxygen-induced orbital hybridization. *Sci. Adv.* **5**, eaax4278 (2019).
131. Lin, W. et al. Enhancement of thermally injected spin current through an antiferromagnetic insulator. *Phys. Rev. Lett.* **116**, 186601 (2016).
132. Zhu, L. et al. Fully spin-transparent magnetic interfaces enabled by the insertion of a thin paramagnetic NiO layer. *Phys. Rev. Lett.* **12**, 107204 (2021).
133. Zhang, J. et al. Band structure and spin texture of Bi_2 Se_3/3d ferromagnetic metal interface. *Phys. Rev. B* **94**, 014435 (2016).
134. Borge, J. & Tokatly, I. V. Ballistic spin transport in the presence of interfaces with strong spin-orbit coupling. *Phys. Rev. B* **96**, 115445 (2017).
135. Rojas-Sánchez, J. C. et al. Spin to charge conversion at room temperature by spin pumping into a new type of topological insulator: α-Sn films. *Phys. Rev. Lett.* **116**, 096602 (2016).
136. Ding, J. et al. Large damping enhancement in dirac-semimetal–ferromagnetic-metal layered structures caused by topological surface states. *Adv. Funct. Mater.* **31**, 2008411 (2021).
137. Miron, I. et al. Perpendicular switching of a single ferromagnetic layer induced by in-plane current injection. *Nature* **476**, 189–193 (2011).
138. You, L. et al. Switching of perpendicularly polarized nanomagnets with spin orbit torque without an external magnetic field by engineering a tilted anisotropy. *Proc. Natl. Acad. Sci. USA* **112**, 10310–10315 (2015).
139. Zheng, Z. et al. Field-free spin-orbit torque-induced switching of perpendicular magnetization in a ferrimagnetic layer with a vertical composition gradient. *Nat. Commun.* **12**, 4555 (2021).
140. Lee, T. et al. Field-free spin-orbit torque switching of GdCo ferrimagnet with broken lateral symmetry by He ion irradiation. *Acta Mater.* **246**, 118705 (2023).
141. Razavi, A. et al. Deterministic spin–orbit torque switching by a light-metal insertion. *Nano Lett.* **20**, 3703–3709 (2020).
142. Wu, H. et al. Chiral symmetry breaking for deterministic switching of perpendicular magnetization by spin–orbit torque. *Nano Lett.* **21.1**, 515–521 (2020).
143. Shu, X. et al. Field-free switching of perpendicular magnetization induced by longitudinal spin-orbit-torque gradient. *Phys. Rev. Appl.* **17**, 024031 (2022).
144. Mac Neill, D. et al. Control of spin–orbit torques through crystal symmetry in WTe_2/ferromagnet bilayers. *Nat. Phys.* **13**, 300 (2017).

145. Han, R. K. et al. Field-free magnetization switching in CoPt induced by noncollinear antiferromagnetic Mn3Ga. *Phys. Rev. B* **107**, 134422 (2023).
146. Liu, Y. et al. Field-free switching of perpendicular magnetization at room temperature using out-of-plane spins from $TaIrTe_4$. *Nat. Electron.* **6**, 732–738 (2023).
147. Mac Neill, D. et al. Thickness dependence of spin-orbit torques generated by WTe_2. *Phys. Rev. B* **96**, 054450 (2017).
148. Peng, C. W., Liao, W. B., Chen, T. Y. & Pai, C. F. Efficient spin-orbit torque generation in semiconducting WTe_2 with hopping transpor. *ACS Appl. Mater.* **13**, 15950–15957 (2021).
149. Li, P. et al. Spin-momentum locking and spin-orbit torques in magnetic nano-heterojunctions composed of Weyl semimetal WTe_2. *Nat. Commun.* **9**, 3990 (2018).
150. Kao, I. H. et al. Deterministic switching of a perpendicularly polarized magnet using unconventional spin–orbit torques in WTe_2. *Nat. Mater.* **21**, 1029–1034 (2022).
151. Liang, S. et al. Spin-orbit torque magnetization switching in $MoTe_2$/permalloy heterostructures. *Adv. Mater.* **32**, 2002799 (2020).
152. Guimaraes, M. H. et al. Spin–orbit torques in $NbSe_2$/permalloy bilayers. *Nano Lett.* **18**, 1311–1316 (2018).
153. Xue, F. et al. Field-free spin-orbit torque switching assisted by in-plane unconventional spin torque in ultrathin [Pt/Co]N. *Nat. Commun.* **14**, 3932 (2023).
154. Nan, T. et al. Controlling spin current polarization through non-collinear antiferromagnetism. *Nat. Commun.* **11**, 4671 (2020).
155. Mahendra, D. C. et al. Observation of anti-damping spin–orbit torques generated by in-plane and out-of-plane spin polarizations in $MnPd_3$. *Nat. Mater.* **22**, 591–598 (2023).
156. You, Y. et al. Cluster magnetic octupole induced out-of-plane spin polarization in antiperovskite antiferromagnet. *Nat. Commun.* **12**, 6524 (2021).
157. Bertaut, E. F., Fruchart, D., Bouchaud, J. P. & Fruchart, R. Diffraction neutronique de Mn_3GaN. *Solid State Commun.* **6**, 251–256 (1968).
158. Matsunami, D., Fujita, A., Takenaka, K. & Kano, M. Giant barocaloric effect enhanced by the frustration of the antiferromagnetic phase in Mn_3GaN. *Nat. Mater.* **14**, 73–78 (2015).
159. Yoon, J. et al. Handedness anomaly in a non-collinear antiferromagnet under spin–orbit torque. *Nat. Mater.* **22**, 1106–1113 (2023).
160. Fukami, S., Zhang, C., DuttaGupta, S. et al. Magnetization switching by spin–orbit torque in an antiferromagnet–ferromagnet bilayer system. *Nat. Mater* .**15**, 535–541 (2016).
161. Huang, Y.-H. et al. A spin-orbit torque ratchet at ferromagnet/antiferromagnet interface via exchange spring. *Adv. Funct. Mater.* **32**, 2111653 (2022).
162. Zhou, J. et al. Chiral interlayer exchange coupling for asymmetric domain wall propagation in field-free magnetization switching. *ACS Nano* **17**, 9049–9058 (2023).
163. Kim, J. H. et al. Field-free switching of magnetization by tilting the perpendicular magnetic anisotropy of Gd/Co multilayers. *Adv. Funct. Mater.* **32**, 2112561 (2022).
164. Bose, A. et al. Tilted spin current generated by the collinear antiferromagnet ruthenium dioxide. *Nat. Electron.* **5**, 267–274 (2022).
165. Ryu, J. et al. Efficient spin–orbit torque in magnetic trilayers using all three polarizations of a spin current. *Nat. Electron.* **5**, 217–223 (2022).

Acknowledgements

This work was supported by the National Natural Science Foundation (52161135103, 52250418, 62131017, 62304120, 2024T170462).

Author contributions

T.X. Nan supervised the project. All authors wrote, reviewed and edited the manuscript.

Competing interests

The authors declare no competing interests.

Additional information

Correspondence and requests for materials should be addressed to Tianxiang Nan.